Chapter 5

5.1 Introduction

In this study the Mg is substituted in the BSFO samples at Fe-site. Mg substitution could affect magneto-electrical and magneto-optical properties by coupling with localized d-shells of the transition metal. Mg^{2+} improves the space modulated spin structure of BFO by increasing the ferromagnetic properties ($2M_r$ = 1.2077 emu/g at room temperature) and even a five-fold increment in magnetization have been detected [Xu *et al.* 2015]. The least value of leakage current with Mg substitution is 8.89 × 10^{-7} A/cm^2 for $Bi_{0.96}Mg_{0.04}FeO_3$ was reported [Lin *et al.* 2020].

In this work polycrystalline bulk samples of $Bi_{0.9}Sm_{0.1}Fe_{1-x}Mg_xO_3$ (x =0.0, 0.025, 0.050, 0.075, and 0.1) perovskite systems were prepared using high energy ball milling or solid-state reaction method. The effect of Mg-substitution on the structure, magnetic, and electrical properties of $Bi_{0.9}Sm_{0.1}FeO_3$ (BSFO) were investigated. The structural stability of the Mg substituted samples is theoretically calculated by tolerance factor using equation 1.1 and graphically shown in fig. 5.1.

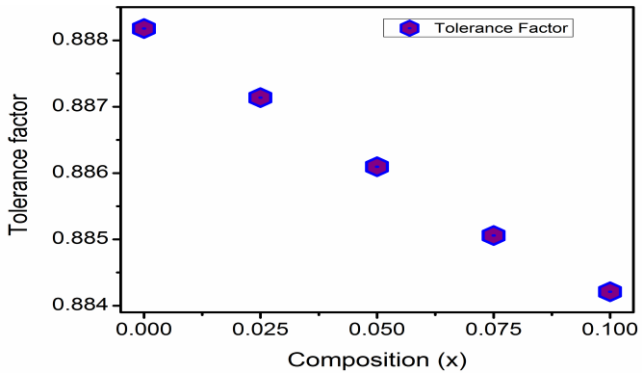

Fig. 5.1: Calculated variation of tolerance factor with composition of samples $Bi_{0.9}Sm_{0.1}Fe_{1-x}Mg_x O_3$ (x =0.0, 0.025, 0.050, 0.075, and 0.1).

5.2 Results

5.2.1 Structural studies and phase identification

Fig. 5.2 shows the X-ray diffractograms of $Bi_{0.9}Sm_{0.1}Fe_{1-x}Mg_xO_3$ (x =0.0 - 0.1 at the step of 0.025) at room temperature. The phase evaluation is done using software X 'pert high score, and all the diffraction peaks indexed matched with the standard $BiFeO_3$ JCPDS file (#86-1518) [Dudarev *et al.*1998, Kum-onsa *et al.* 2020]. The most intense reflection peaks (104) and (110) are recorded at diffraction angles $2\theta \approx 32°$ signifying the major phase present in all the compounds is Rhombohedral with R*3c* space group symmetry. Further, this major peak (110/104) corresponding to $2\theta \sim 32^o$ is observed to merge with the increase in x, as shown in Fig. 5.2 (b). A small secondary phase is observed at x =0.0, and with the increase in x (Mg substitution), some more impurity phases appear. The intensity of the secondary phase at $2\theta \sim 27.5^o$ is observed to increase with *x*, and this belongs to $Bi_{25}FeO_{40}$ the garnet phase/ Fe_2O_3 /$MgFe_2O_4$ as according to JCPDS files, a clear overlapping is observed there. Further, if the intensity of the garnet phase increases, then magnetization should increase, which is not observed in the present case (discussed later in the magnetization case). If $MgFe_2O_4$ intensity increases with x, then leakage current should increase further not observed there [Tan *et al.* 2008]. Thus, according to the Neumann principle, Fe_2O_3/Fe_3O_4 possibility can be there. Fig.5.2 (c) shows the X-ray diffractograms of the secondary phase corresponding to $2\theta \sim 32.5^{o,}$ which shows that the intensity of the secondary phase increases with *x* and is also observed to shift with x. This shows that the secondary phase belongs to Fe_2O_3 as with the Mg substitution, Mg has entered the lattice and compelled Fe to come out of the lattice.

This is further confirmed through the titling and buckling of FeO_6 octahedra, and the change in bond angle from 153.95^o to 155.75^o obtained using cif files extracted from Rietveld

refinement (Fig. 5.2 (d)). Further, the buckling of FeO_6 octahedra has to lead to the merging of peaks [Brahmi *et al.* 2016, Singh *et al.* 2015].

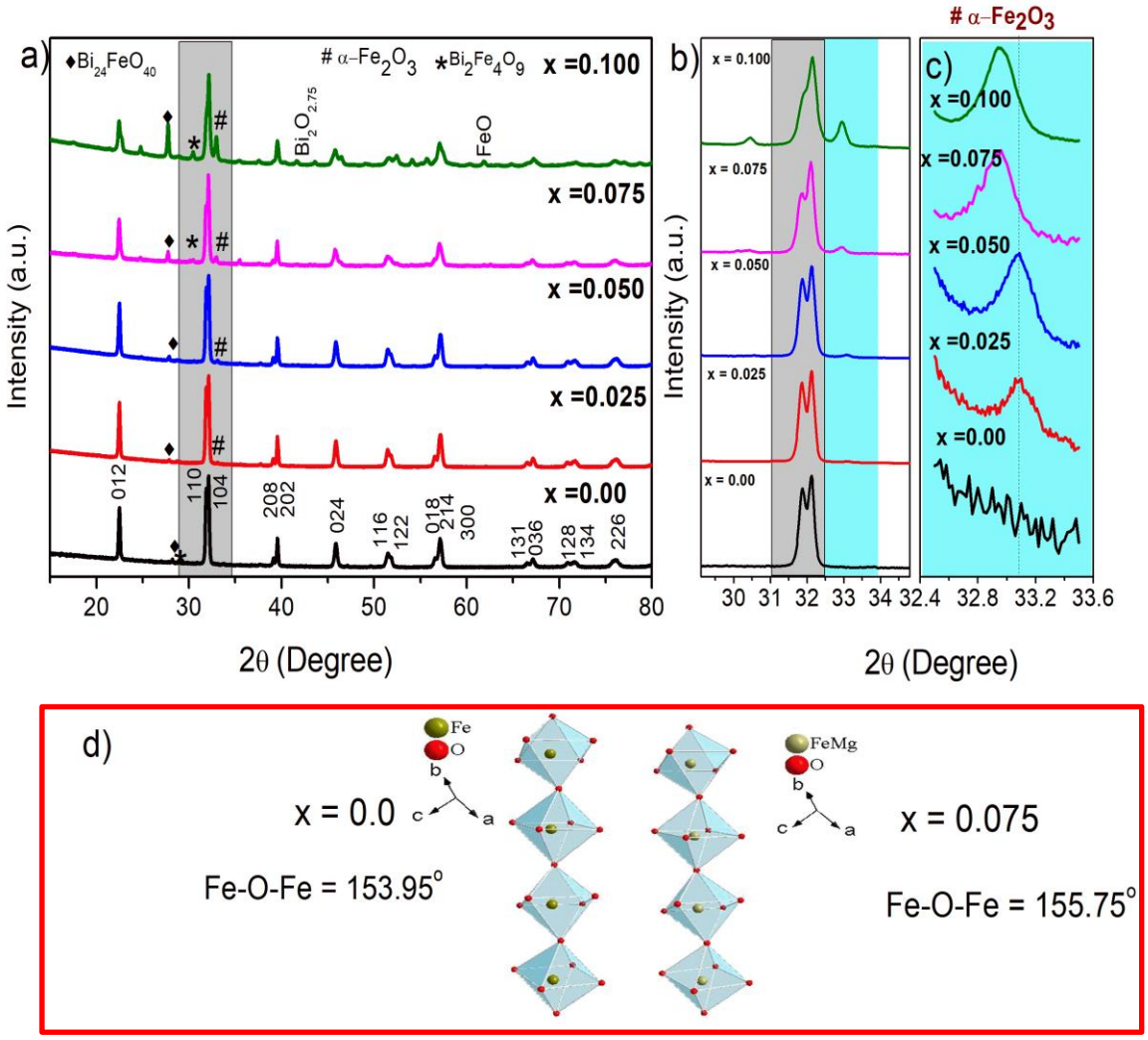

Fig. 5.2 (a): XRD graphs of $Bi_{0.9}Sm_{0.1}Fe_{1-x}Mg_xO_3$ (x =0.0, 0.025, 0.050, 0.075, and 0.1); **(b)** Magnified pattern of peaks (110) and (104); **(c)** Magnified pattern of the secondary phase (Fe_2O_3).

The crystallographic information of Mg-substituted BSFO systems was accomplished with Rietveld refinement using the FULLPROF software shown in Fig. 5.3 (a-d). It is observed that all the XRD patterns are fitted with single phase R*3c* symmetry. A minor

impurity phase of Fe_2O_3 is observed but the primary phase was rhombohedral, and the data obtained from refinement is in an acceptable range. Due to enhanced impurity phases in the XRD data, the results for $x = 0.10$ won't discuss for further investigations.

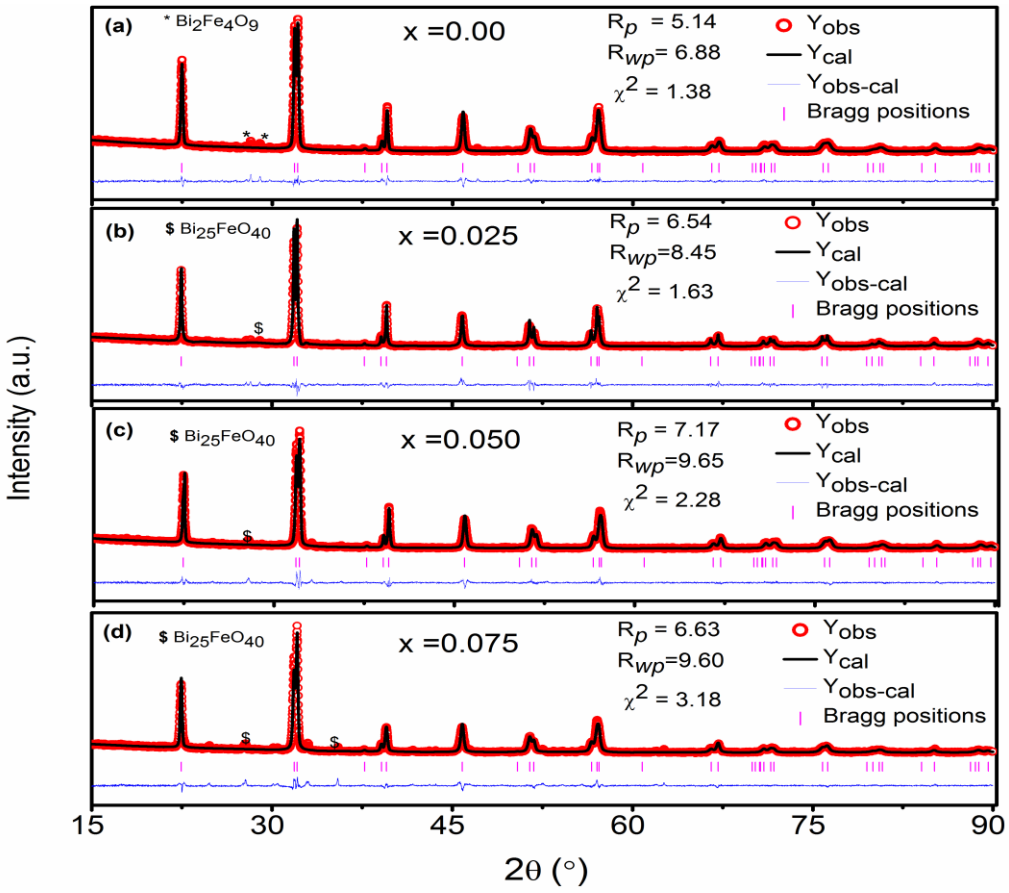

Fig. 5.3 (a-d): Rietveld refinement of $Bi_{0.9}Sm_{0.1}Fe_{1-x}Mg_xO_3$ series with x = 0.0, 0.025, 0.050, and 0.075.

From the refined structure of all the samples, lattice parameters and Fe-O bond length were calculated and plotted concerning the composition shown in Fig. 5.4(a). Fig. 5.4(b) shows the arrangement of atoms in the parent BFO structural unit cell. Fig. 5.4(a) shows that the bond length decreases, and lattice parameter '*c*' increases up to x =0.05 due to the larger ionic radii of Mg^{2+} (0.72 Å) as compared to Fe^{3+} (0.64 Å) which results into larger displacement of Fe

cations from the center plane between the Bi sublattices. After x ≥ 0.075, the lattice parameter decreases while the bond length increases; this is due to the Mg concentration reached to its solubility limit [Li *et al.* 2016, Notonegoro *et al.* 2019]. The type and effect of bonding have been discussed in detail in the FT-IR section.

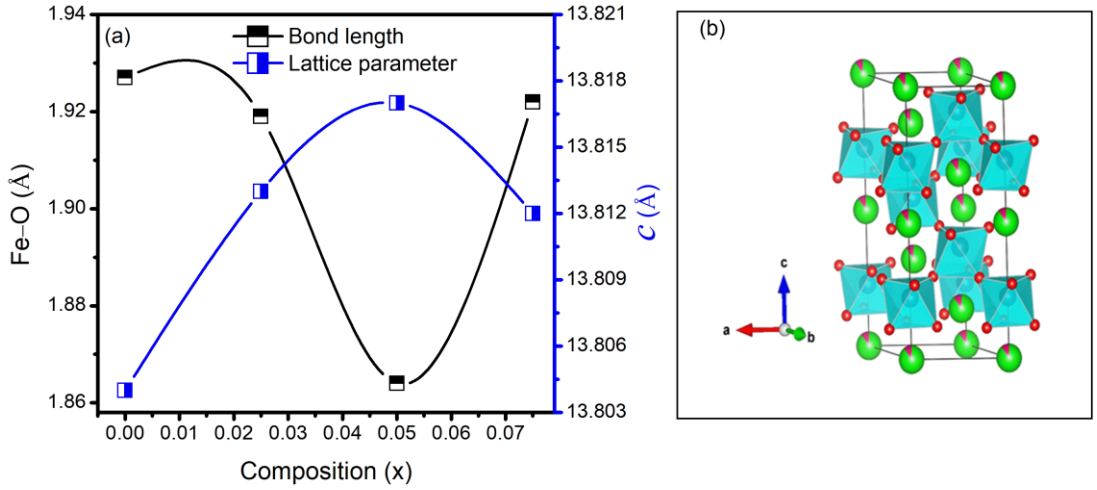

Fig. 5.4: (a) Bond length (Fe-O) variation with the composition of $Bi_{0.9}Sm_{0.1}Fe_{1-x}Mg_xO_3$; x =0.0, 0.025, 0.050, and 0.075; **(b)** Crystal structure of pure BSFO sample in which different atoms are shown with different colors (red O- ions, green-Bi/Sm, inside of blue octahedra are Fe-ions).

5.2.2 FT-IR Studies

Fig. 5.5 shows the room temperature FT-IR spectra of all the Mg-substituted samples obtained in the range of 400 - 1000 cm^{-1}. The most effective absorptive peak is recorded for $Bi_{0.9}Sm_{0.1}Fe_{1-x}Mg_xO_3$ (x =0.0, 0.025, 0.050, 0.075) at wavenumbers ~559 cm^{-1}, ~563 cm^{-1}, ~565cm^{-1}, ~561 cm^{-1} respectively are corresponding to stretching and bending vibration of Fe-O bond. It is due to the existence of FeO_6 octahedra along with the (Bi 6sp - O 2p) complex group [Singh *et al.* 2012]. The Fe-O bond position shifts towards a higher

wavenumber and a Fe-O bond length decrease with x is due to the distortion of FeO_6 octahedra. This octahedra tilting affect the superexchange interaction by varying the oxygen vacancies and variation Fe^{2+}/Fe^{3+} content.

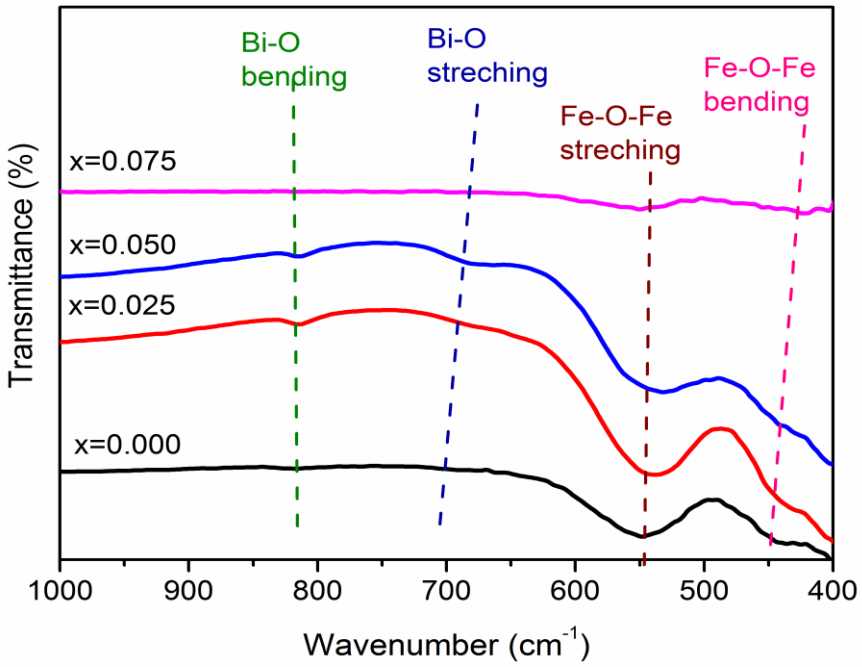

Fig. 5.5: FT-IR spectra of $Bi_{0.9}Sm_{0.1}Fe_{1-x}Mg_xO_3$ series with x =0.0, 0.025, 0.050, and 0.075.

The absorption peaks ~690 cm^{-1} correspond to Bi-O stretching, and the peaks ~811 cm^{-1}, ~810 cm^{-1}, ~790 cm^{-1} correspond to the bending vibration mode of Bi_2O_3. The existence of metal oxide bands confirms the formation of the perovskite structure in the samples [Gowrishankar *et al.* 2016]. Also, the force constant and bond length of the studied samples are illustrated in Table 5.1. The vibration frequency of the Fe-O bond can be determined by using the equation (5.1):

$$\nu = \frac{1}{2\pi c}\left(\frac{k}{\mu}\right)^{1/2} \qquad (5.1)$$

Where ν is the wavenumber, c is the velocity of light (3×10^8 m/s), *k* is the average force constant of Fe-O bond and μ is effective mass, which can be given by equation (5.2):

$$\mu = \frac{A_O \times A_{Fe}}{A_O + A_{Fe}} \quad (5.2)$$

Where A_O and A_{Fe} are the atomic weight of O and Fe, respectively. The force constant can be calculated by the following equation (5.3):

$$k = \frac{17}{r^3} \quad (5.3)$$

Where r is the bond length.

Table 5.1 Wavenumber, effective mass, force constant, bond length calculated from FTIR; Bond angle calculated from Rietveld.

Composition	Wave no. (cm^{-1})	Effective mass (10^{-26} Kg)	Force constant *k* (N/cm)	Bond length (Fe-O) (A°) {from FTIR}	Bond Angle {from Rietveld}
x = 0.000	559.33	2.06	2.20	1.95	153.9 (7)
x = 0.025	563.19	2.06	2.23	1.94	156.3 (7)
x = 0.050	565.12	2.06	2.25	1.94	154.3 (9)
x = 0.075	561.26	2.06	2.21	1.94	155.7 (2)

5.2.3 Microstructural studies with scanning electron microscopy

Fig. 5.6 (a-d) shows the typical back scattered micrographs of all the samples, recorded at a scale of 1 μm and 50,000 magnifications to analyze the formation of secondary phases.

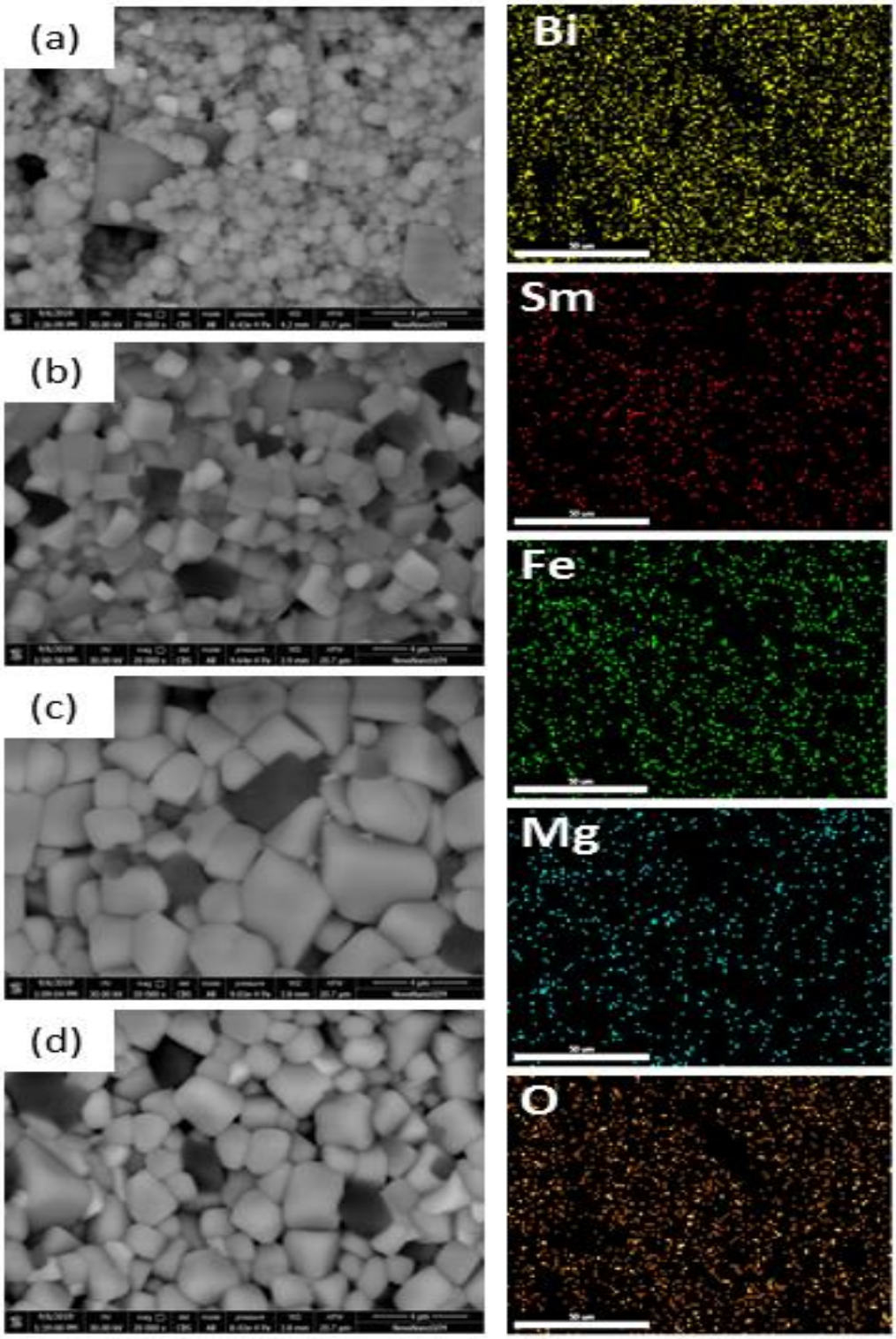

Fig. 5.6 (a-d): BSE images of $Bi_{0.9}Sm_{0.1}Fe_{1-x}Mg_xO_3$ with x =0.0, 0.025, 0.050, and 0.075.

Besides images show elemental mapping of sample with x = 0.05.

Also, the elemental distribution of Bi, Sm, Fe, Mg, and O respectively shown by EDS mapping recorded at a scale of 2 μm. All the elements are almost uniformly dispersed in BFO matrix. The polycrystalline grains are randomly oriented in all the back-scattered micrographs. It is observed that the grain growth increases with the Mg substitution content (x =0.05), and also, some of the grains grow abnormally in the range of 1μm - 2.8μm. A generally responsible factor for abnormal grain growth is step-free energy.

The mechanism is the step-free energy reduced by increasing step-growth, which in turn enhances the boundary movement by roughening transition, as the boundary movement varies from one boundary to another, so the driving force increased so, the growth of smaller grains suppressed, and some of the grains grow unusually [Singh *et al.* 2020].

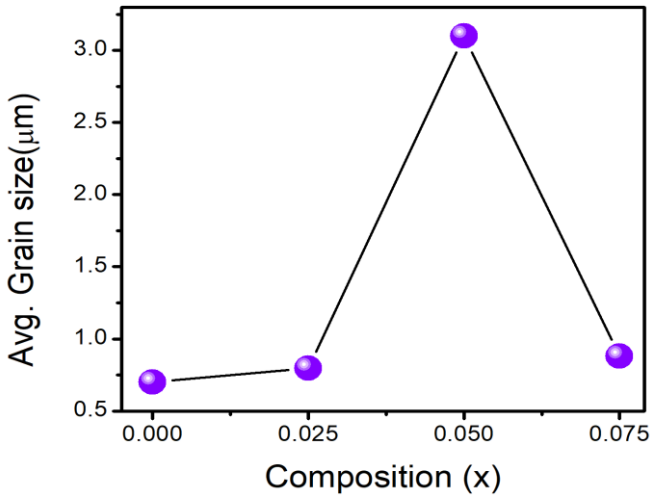

Fig. 5.7: Average grain size variation with the composition.

Fig. 5.7 shows the variation of grain sizes with the Mg substitution in the BSFO. It is noticed that the average grain sizes enhance with increasing magnesium substitution this is due to the contribution of bismuth-rich minor impurity phases, which were also detected with XRD. To compensate the bismuth deficiency and to maintain charge neutrality, grain

boundaries get drifted [Jung *et al.* 2007]. The grain boundaries drift due to the alteration in driving force and chemical potentials associated with bismuth cation and oxygen vacancies. Thus, the reduction in grain size for higher composition x =0.075 is the creation of vacancies at the grain boundary, and different grain/grain-boundary elemental concentrations might lead to recrystallization and grain growth [Chen *et al.* 2019].

5.2.4 X-ray photoelectron spectroscopy

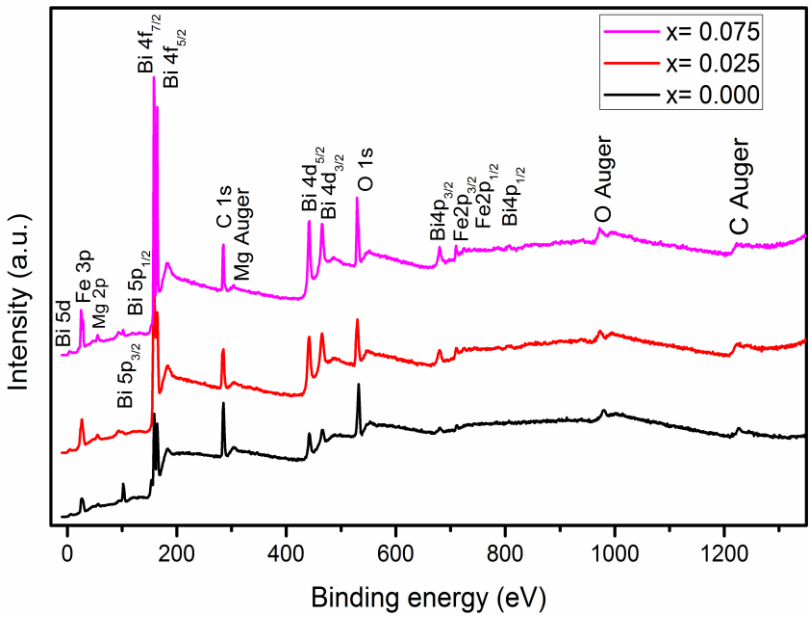

Fig. 5.8: XPS complete survey of samples $Bi_{0.9}Sm_{0.1}Fe_{1-x}Mg_xO_3$ (x =0.0, 0.025, and 0.075).

Fig. 5.8 shows a wide scan XPS survey of Mg-substituted BSFO samples to identify the oxidation state, chemical shift of elements, and oxygen vacancies. The charging correction of carbon =286.8 was made for obtaining the binding energy of all the samples. For detailed analysis narrow scanned, Gaussian fitted spectra of Fe 2p and O 1s orbitals for $Bi_{0.9}Sm_{0.1}Fe_{1-x}Mg_xO_3$ (x =0.0, 0.025, 0.050, 0.075) samples are shown in Fig. 5.9.

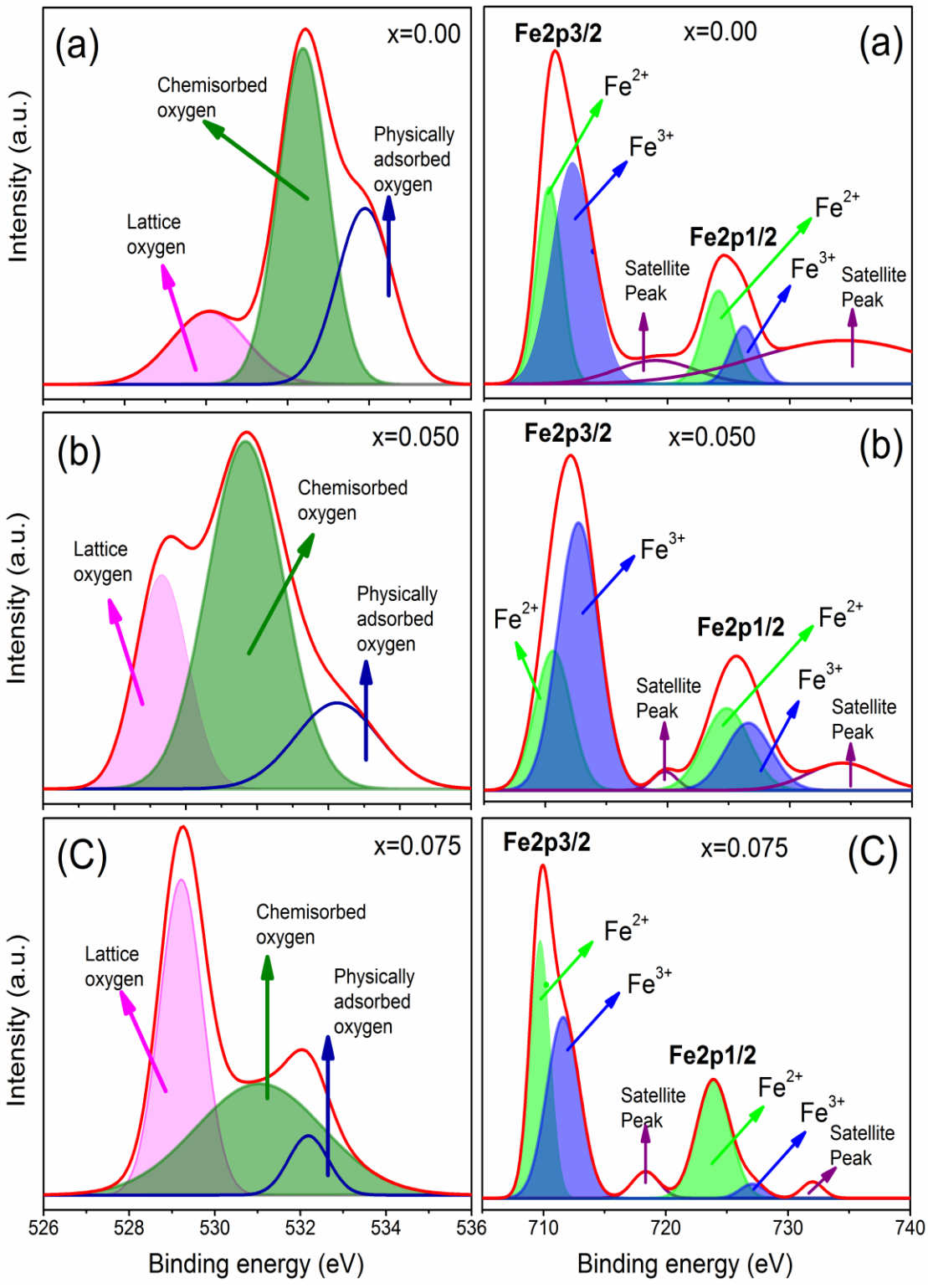

Fig. 5.9: Gaussian fitted XPS spectra of Fe and O elements of samples $Bi_{0.9}Sm_{0.1}Fe_{1-x}Mg_xO_3$ (x =0.0, 0.025, 0.050, and 0.075).

Fig. 5.9 (a-c left) shows high-resolution orbital spectra of O1, which is discerned into three peaks in the range of about ∼529, ∼531, ∼533, corresponding to lattice oxygen, chemisorbed oxygen, and physically adsorbed oxygen, respectively. The lattice oxygen corresponds to the oxygen content, and chemisorbed oxygen refers to the hydroxide bond or the oxygen vacancy content [Singh *et al.* 2020]. It is observed that oxygen vacancy is minimum at x =0.075 while maximum vacancy is at x =0.05. Further, it is noticed that the intensity of physically adsorbed oxygen or auger peaks decreases with *x*, suggesting the transfer of an electron from the vacant d-orbital.

5.9 (a-c right) shows the Fe 2p doublet, Fe $2p_{3/2}$ ∼709.63 eV and Fe $2p_{1/2}$ ∼723.26 eV; arising from spin-orbital splitting. Spin-orbit splitting energy is equal to 13.63 eV, equivalent to the theoretical value of Fe 2p (13.6 eV) for Fe_2O_3 in literature. In order to explain the behavior of Fe in the Mg doped samples the intensity ratio of Fe2p3/2 to Fe2p1/2 calculated and shown in table 5.2 and compared with Fe content calculated from EDX data as shown in table 5.3. It is observed that with the addition of Mg^{2+}, the intensity of Fe^{2+} is observed to increase at x =0.075 and minimum Fe^{2+} intensity is observed at x =0.05. Besides, two satellite peaks were observed at ∼720eV and ∼725eV that further confirms the 3+ oxidation state of Fe in BSFO samples. The intensity of the satellite peak is observed to decrease with *x* and in correlation with the O Auger peak suggesting the transfer of d-electron from the partially filled d-orbital to the vacant orbital, leading to the superexchange interaction. Further, the chemisorbed oxygen position is observed to shift left at x =0.05 and then shift right for x =0.075, suggesting the change in oxidation state from O^{-2} to $O^{-2-\delta}$. This is in accordance with the shifting of Fe^{2+} and Fe^{3+} leading to the transformation in the oxidation state.

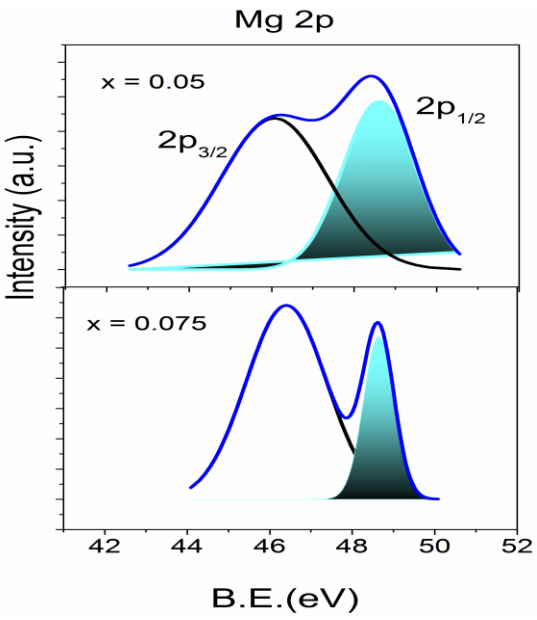

Fig. 5.10: Gaussian fitted XPS spectra of Mg for samples $Bi_{0.9}Sm_{0.1}Fe_{1-x}Mg_xO_3$ (x =0.050 and 0.075).

Table 5.2 Findings from XPS data

Sample	Peak Index	Area	Intensity	Intensity ratio
BSFO	Fe2p3/2 Fe^{2+}	3526.73	1354.67	1: 1.1
	Fe2p3/2 Fe^{3+}	6476.97	1525.86	
	Satellite Peak 1	1311.62	162.05	
	Fe2p1/2 Fe^{2+}	1979.51	641.68	
	Fe2p1/2 Fe^{3+}	1097.36	396.01	
	Satellite Peak 2	4372.58	299.61	
Mg=0.05	Fe2p3/2 Fe^{2+}	13537.41	3667.54	1:1.9
	Fe2p3/2 Fe^{3+}	29653.69	7036.76	
	Satellite Peak 1	1216.01	494.52	

	Fe2p1/2 Fe^{2+}	10175.67	2159.87	
	Fe2p1/2 Fe^{3+}	8368.76	1773.27	
	Satellite Peak 2	4990.23	714.62	
Mg=0.075	Fe2p3/2 Fe^{2+}	14377.08	8304.77	1:1.2
	Fe2p3/2 Fe^{3+}	33578.32	9215.37	
	Satellite Peak 1	2883.97	1060.21	
	Fe2p1/2 Fe^{2+}	9639.96	3942.19	
	Fe2p1/2 Fe^{3+}	10324.97	2615.30	
	Satellite Peak 2	4633.52	893.46	

Table 5.3 Fe content from EDX data

Samples	**Fe content**
x = 0.000	17.88
x = 0.025	20.24
x = 0.050	17.03
x = 0.075	22.84

For the confirmation of Mg estimation, deconvoluted XPS spectra of Mg are plotted in Fig. 5.10. According to the standard XPS lookup table, the prominent Mg 2p peak is indexed at 49-50eV. We have observed that the intensity of Mg $2p_{3/2}$ peak is higher at x =0.075 than at x =0.05 while the intensity of $2p_{1/2}$ reduces at x =0.075. This is suggesting the increase in +2 state at x =0.075 rather than at x =0.05 evidenced from EDX data also.

5.2.5 Magnetic studies

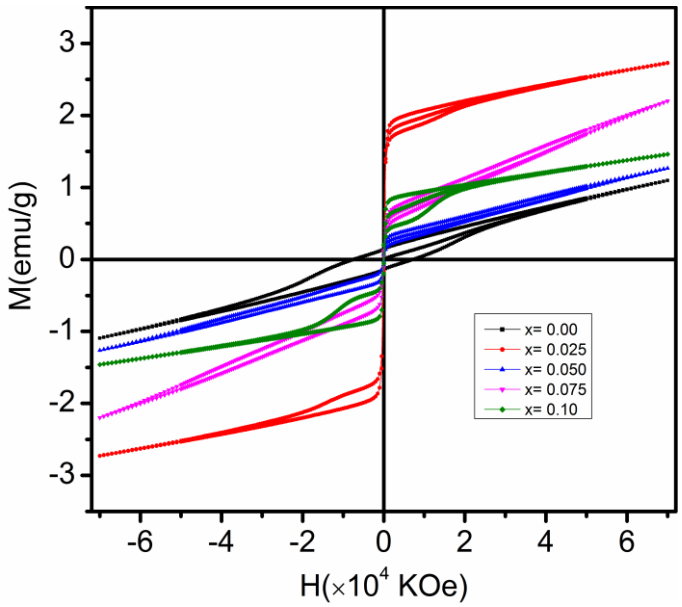

Fig. 5.11: Hysteresis curves of samples of $Bi_{0.9}Sm_{0.1}Fe_{1-x}Mg_xO_3$ (x =0.0, 0.025, 0.050, and 0.075).

Fig. 5.11 shows the variation of magnetic moment with the applied magnetic field for all the sintered samples recorded at room temperature. The Mg-substituted BSFO samples show an antiferromagnetic behavior; however, a remarkable magnetic moment enhances up to x =0.050 due to increasing Fe^{3+} content and higher oxygen vacancies as seen through XPS. After that contribution of Fe^{2+} valency increases, which results in decreasing the magnetic moment.

5.2.5.1 Effect of temperature on Magnetization

Fig. 5.12 shows effect of temperature on the magnetization on $Bi_{0.9}Sm_{0.1}Fe_{1-x}Mg_xO_3$ (x =0.0, 0.025, 0.050, 0.075) samples. Mg-substituted antiferromagnetic samples follow Brillouin-like

behavior [Bharathi *et al.* 2011]. This Brillouin behavior is described by fitting ZFC data of all the samples with the logistic function equation (5.4).

$$Y = \frac{M_1 - M_2}{1+(T/T_0)^n} + M_2 \quad (5.4)$$

Where, M_1 and M_2 are Magnetic moments; T_o = temperature; n = temperature exponent.

Table 5.4 Magnetic moment, temperature calculated from logistic Equation.

Samples	**x =0.025**	**x =0.050**	**x =0.075**
M_1	1.17	0.12	0.18
M_2	0.73	0.09	0.12
T_0	392.38	359.43	317.34
n	2.69	2.95	2.82

The Brillouin behavior is explained in detail for x =0.05, shown in Fig. 5.13. The blue line shows the reversible region, which has a positive slope segment and is weakly dependent on temperature. The irreversible temperatures (T_{irr}) of all Mg-substituted ZFC curves are ~252K, ~272K, and ~259K, for x =0.025, 0.050 and 0.075 respectively. Also, it observed that ZFC moments are increasing with decreasing temperature and show maxima ~8K; it is blocking temperature for all the samples denoted by T in the image. It is noticed that at ~285 K, there is a crossover point, which may be the Curie temperature (T_c) of any element substituted in the compound [Harrison *et al.* 2014]. Further, from Fig. 5.12, it is observed that the fitting could not be achieved for pure BSFO samples while Mg substituted samples fitted successfully. The values of magnetic moment and temperature obtained for (x =0.025, 0.050, 0.075) calculated from equation (5.4) are shown in table 5.4.

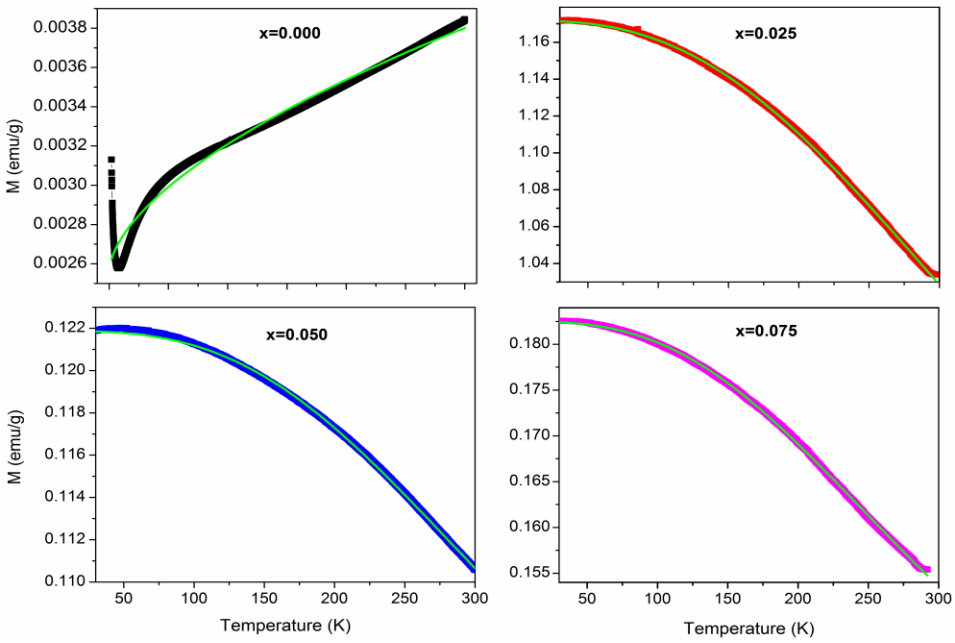

Fig. 5.12: ZFC curves of $Bi_{0.9}Sm_{0.1}Fe_{1-x}Mg_xO_3$ (x =0.0, 0.025, 0.050, and 0.075) fitted using logistic function.

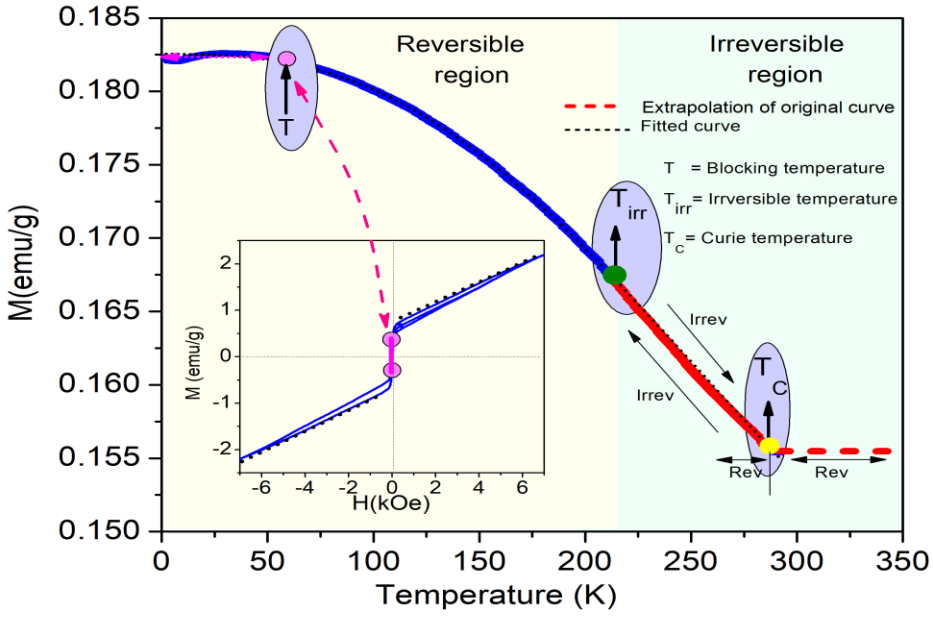

Fig. 5.13: Brillouin behavior is explained by the fitted ZFC curve for Mg content x =0.05.

However, as per the earlier report, this Brillouin behavior is expected due to the oxygen vacancies and Fe^{2+}/Fe^{3+} variation. This results in domain pinning, which alters the magnetization in Mg substituted samples. Thus, Mg substituted samples are expressed by Brillouin behavior.

5.2.6 Impedance behavior

Fig. 5.14 shows the Modulus Nyquist plots at 370 ^{o}C (around Neel temperature) where M' and M" are calculated by the relations $M' = \omega C_o Z''$ and $M'' = \omega C_o Z'$ to suppress the electrode effect and to get information about homogeneity/ inhomogeneity of the polycrystalline samples [Das *et al.* 2012]. Normally, in the modulus spectrum, an electrical phenomenon with small capacitance is observed. But, in the present case, the diffusive structure with some defects is observed in the modulus plots. However, the capacitance is more in x =0.05 and is two orders higher than x =0.0 sample.

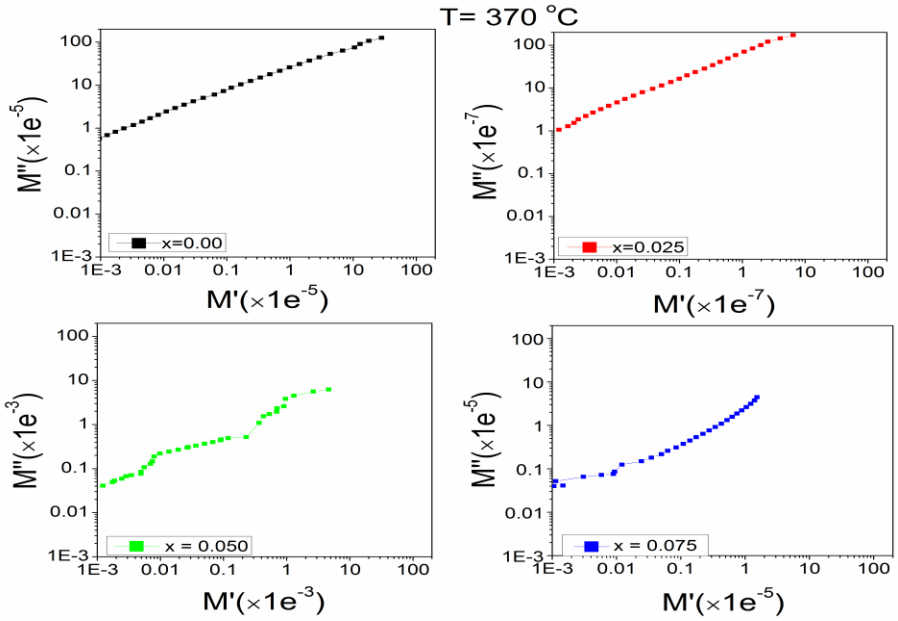

Fig. 5.14: M' vs M" plots at temperature 370 °C (643 K) of $Bi_{0.9}Sm_{0.1}Fe_{1-x}Mg_xO_3$ (x =0.0, 0.025, 0.050, and 0.075).

In order to find the increase in the cause of polarization, an imaginary part of the modulus is plotted versus the log of frequency (ω) in Fig. 5.14. It is observed that at low frequency, a small peak is observed while there is no peak at higher frequencies. In addition, the peak at low frequency and low temperatures diminishes at higher temperatures. Further, peak shifting indicates the correlated motion of charge carriers with conductivity relaxation, and asymmetricity indicates the non-Debye type behavior with different time constants. The low-frequency peaks indicate the long-distance movement of ionic charge carriers [Priyanka *et al.* 2013].

Further, activation energy is plotted using the Arrhenius equation shown in the Inset of Fig. 5.15. It is observed that the activation energy lies in the range of 0.1- 0.3eV in the temperature range of RT – 500 ^{o}C. As seen in the plots, there are three slopes due to the different anomalies well known for $BiFeO_3$. This suggests that the x =0.05 sample has higher polarization with hopping relaxation of singly ionized oxygen vacancies.

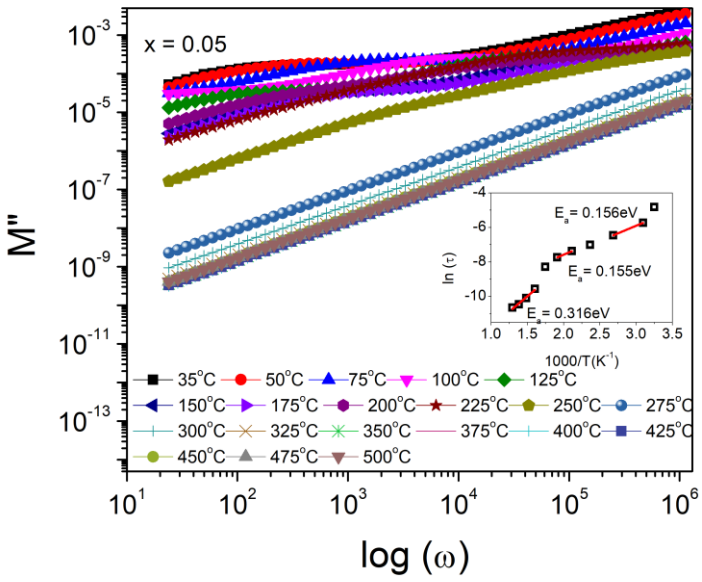

Fig. 5.15: M'' Vs. log (ν) plot for x= 0.05. Inset shows the activation energy plot of the same.

5.2.7 I-V characteristics

Fig. 5.16 shows the curves of leakage current density as a function of applied voltage for all the studied samples. It is observed that the leakage current decreases dramatically with the increasing Mg content up to x =0.050 and then enhances. The values of leakage current density are obtained for all the samples of $Bi_{0.9}Sm_{0.1}Fe_{1-x}Mg_xO_3$ (x =0.0, 0.025, 0.050, 0.075) are as 1.37, 3.87×10^{-4}, 3.64×10^{-7}, and 5.48×10^{-4} respectively at 60 kV/cm applied field.

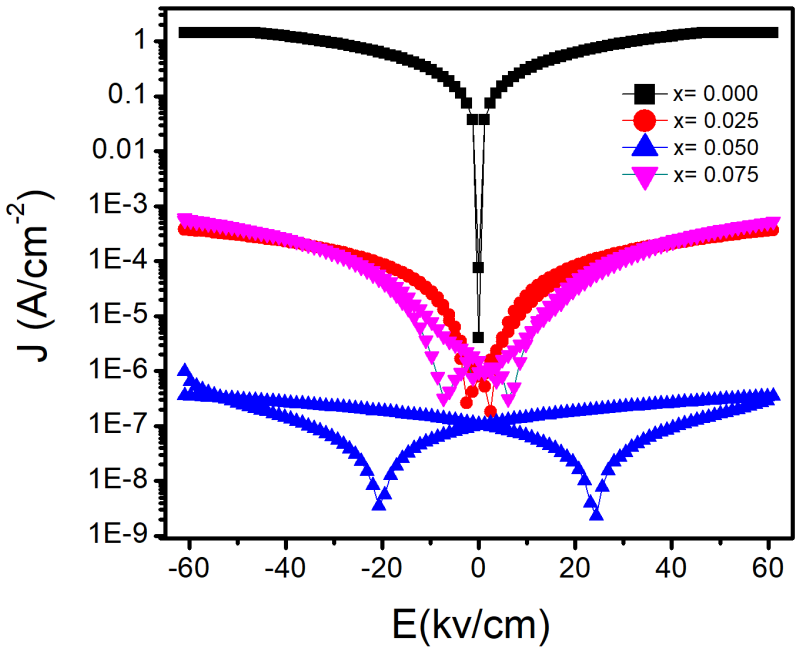

Fig. 5.16: (a)Current density variation with applied voltage of the samples of $Bi_{0.9}Sm_{0.1}Fe_{1-x}Mg_xO_3$ (x =0.0, 0.025, 0.050, and 0.075).

5.2.7.1 Leakage current understanding based on XPS analysis

The leakage current density depends on the creation of oxygen vacancy, and also, the exchange ion interaction plays a vital role in the electrical properties [Wu *et al.* 2011]. The mechanism behind the leakage current is explained from the following equations:

$$O'' \leftrightarrow V_O^{\cdot\cdot} + 2e'$$

$$Fe^{\cdots} + e' \leftrightarrow Fe^{\cdot\cdot}$$

$$O_O^{\times} + 2Fe^{\cdots} \leftrightarrow 2Fe^{\cdot\cdot} + V_O^{\cdot\cdot} \quad (5.5)$$

Bi leads to impurity phases due to its highly volatile nature and oxygen vacancies, which created Fe^{2+} ions in BSFO samples. From XPS data, it can be described that with increasing the magnesium concentration, the oxygen vacancies come to the lattice again, and Fe^{2+} gets oxidized to Fe^{3+} ions, which support leakage current density up to x =0.050, and then the inclusion of impurity phases increases both the lattice oxygen and Fe^{2+} ions concentration.

5.2.7.2 Leakage current understanding based on thermodynamics

The substitution of Mg^{2+} ions at the Fe-site of the BSFO system enhances the resistivity of the material. There are several reported mechanisms for measurement of DC electrical properties of substituted cations in $BiFeO_3$, such as space charge limited conduction (SCLC), grain boundary limited conduction, Schottky emission, Pool-Frenkel emission, and Fowler-Nordheim tunneling, Ohmic conduction [Sharma *et al.* 2019, Singh *et al.* 2015]. In a bulk material, the conduction mechanism mainly depends on the density of the charge carriers. Ohmic conduction and SCLC are dependent on the density of the charge carriers present in bulk and the charge carriers injected from the electrodes. The Ohmic conduction is dominating when the density of the injected charge carriers from the electrodes is lower than the density of charge carriers in bulk. SCLC prevailed when the density of charge carriers in bulk is lower than the density of the injected charge carriers from the electrodes.

The conduction mechanisms obey the power law: $J \propto E^{\alpha}$. The value of α is the slope of the ln (J) versus ln (E) plot shown in Fig. 5.17. The value of $\alpha < 1$for grain boundary limited conduction; $\alpha = 1$ for Ohmic conduction; and $\alpha \leq 2$ for space charge limited conduction. The grain boundary is limited, and Ohmic conductions are dominating in almost all samples. The decreasing slope is due to the increasing lattice parameters, which signify the decrement in the oxygen vacancies. For x =0.075, the SCLC mechanism and grain boundary limited conduction were competing, so leakage current increases. Lattice parameters also decreased.

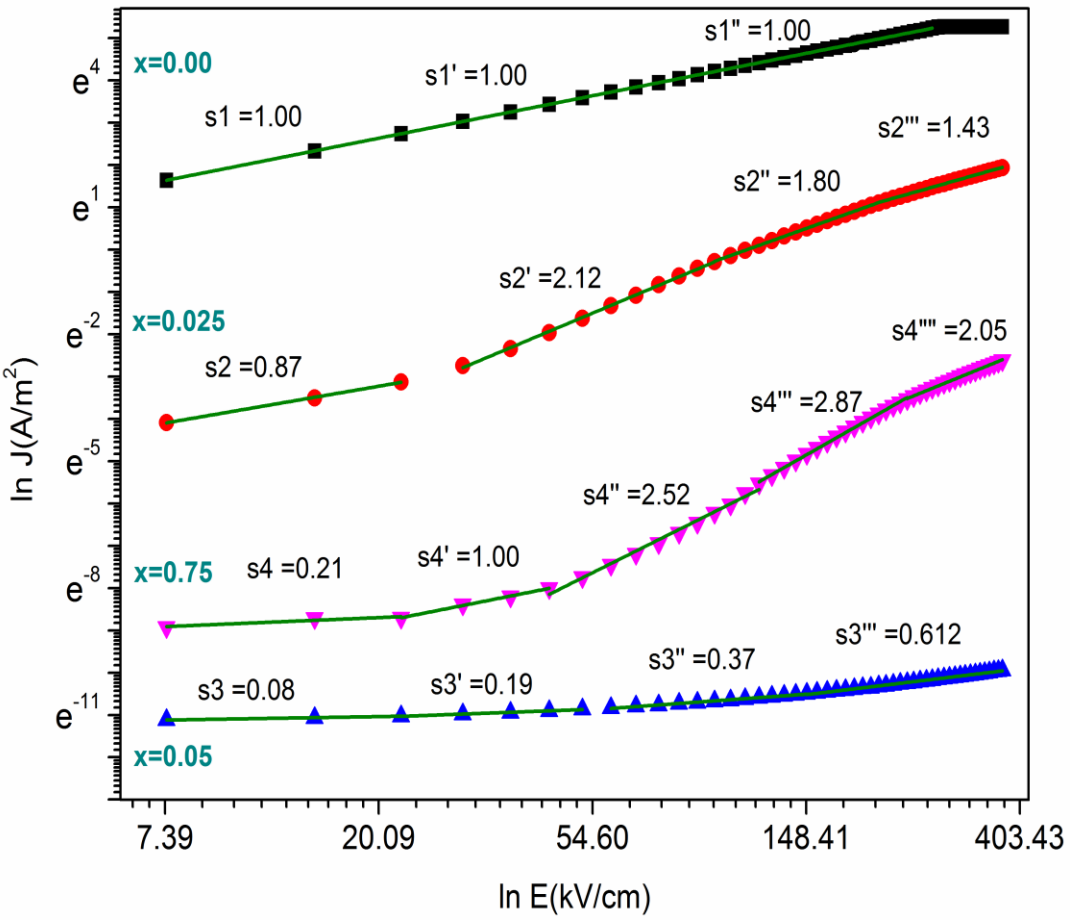

Fig. 5.17: ln J vs. ln E linearly fitted curves of the $Bi_{0.9}Sm_{0.1}Fe_{1-x}Mg_xO_3$ (x =0.0, 0.025, 0.050, and 0.075) samples.

5.3 Summary

Summarily Mg substituted samples are observed in a single phase with R3c symmetry. This work deals with an easy and industrially adoptable (solid-state) synthesis process along with an insight into the relationship between temperature-dependent magneto-dielectric properties. For Mg substituted $Bi_{0.9}Sm_{0.1}FeO_3$ (BSFO) system, which results in enhanced magnetic and electrical properties with least leakage current value is 3.64×10^{-7} A/cm^2 reported for $Bi_{0.9}Sm_{0.1}Fe_{0.95}Mg_{0.05}O_3$, which is comparatively lower than reported for thin films (8.89×10^{-7} A/cm^2) [Lin *et al.* 2020] and comparable with samples prepared using rapid sintering method (2.1×10^{-7} A/cm^2) [Xi *et al.* 2014]. The grain boundary limited conduction, and Ohmic conductions were dominating in almost all samples. The as-prepared material can be a good choice for various applications such as nonvolatile ferroelectric random access memory, magnetic data storage, and other electron device applications.